Storm-Forced Baroclinic Near-Inertial Currents on the Grand Bank

BRAD DE YOUNG* AND C. L. TANG

Physical and Chemical Sciences, Scotia-Fundy Region, Department of Fisheries and Oceans, Bedford Institute of Oceanography, Dartmouth, Nova Scotia, Canada

(Manuscript received 17 May 1989, in final form 12 April 1990)

ABSTRACT

Current meter data for six months from the Grand Bank are analyzed to study inertial currents generated by moving storms. It is found that during periods of strong winds, but no well-defined storm system, the inertial motion exhibits no simple relationship to the local wind. During intense storms inertial currents up to 0.5 m s^{-1} were observed both in and below the mixed layer. Upper and lower layer currents are roughly equal in amplitude, but are 180° out of phase. To explain this observation, a two-layer, one-dimensional model is developed that successfully simulates the observed inertial currents. We show that under the conditions encountered during the storms only baroclinic inertial motion can be generated. The pressure gradient effect is not important, and the current below the mixed layer is produced by mass continuity. Wavelength computed from the continuity equation is consistent with that predicted by first-order linear theory. For inertial motion generated during periods of strong wind but no cyclone, pressure gradients and barotropic response can be important and should not be neglected.

1. Introduction

Wind generation of inertial motion has been investigated by many authors since the pioneering work of Veronis (1956). There are different approaches to the problem depending on the objective of an investigation. For ocean current research on the Grand Bank, a major goal is to develop methods to hindcast currents on time scales from half-day to several days in response to intense storms, using available environmental data. Towards this goal a field program was launched in 1986 to collect current and hydrographic data in the northwestern Grand Bank where the Hibernia oil field (47°N, 49°W) is located. This paper presents the results of an analysis of this dataset. The objective is to model inertial currents, during periods of intense storms, both in and below the mixed layer using winds at a single point. The focus of the paper is currents at near-inertial frequency, which for simplification we shall call inertial currents. Apart from generating inertial currents, storms can cause deepening of the mixed layer and drive nonoscillatory currents, which may have an amplitude comparable to or greater than that of inertial currents. These are important topics in storm research but are beyond the scope of this investigation. In this paper we shall remove nonoscillatory motion by filtering, and treat the mixed-layer depth diagnostically by using the mixed-layer depth derived from thermistor chain data as input to a model.

The general properties of inertial motion in the wake of a moving storm have been studied by many investigators using two or three dimensional numerical/analytical models (Geisler 1970; Chang and Anthes 1978; Price 1983). To simulate observed inertial currents with single-point winds, a well-known method is that of Pollard and Millard (1970) in which the problem is reduced to one-dimensional form by dropping the pressure gradient terms in the momentum equations, and the wind forcing is assumed to act as a body force distributed uniformly within the mixed layer. Inertial currents produced by this class of models are confined to the mixed layer because there is no mechanism to transfer the inertial energy into the lower layers. In general, there are two ways to generate inertial current in the lower layers: (i) pressure gradients in the mixed layer can be transmitted to the lower layers driving currents there and (ii) mass continuity can force currents in the lower layers even if the pressure gradient is absent or negligibly small.

Much of the work on inertial oscillation below the mixed layer has focused on vertical propagation of inertial wave energy from the surface to the ocean interior (Kroll 1975; Tang 1979; Gill 1984; Kundu and Thomson 1985; Shay and Elsberry 1987; D'Asaro 1987). Vertical propagation is a consequence of pressure gradient effects and is a major contributor to inertial wave energy in the deep ocean. However, realistic event sim-

* Present affiliation: Department of Physics, Memorial University of Newfoundland.

Corresponding author address: Dr. Brad de Young, Department of Physics, Memorial University of Newfoundland, A1B 3X7 Canada.

ulation incorporating the pressure gradient effects is difficult because pressure gradients are determined not only by the local wind field, but are also influenced by conditions at great distances. Pressure gradients are also notoriously difficult to measure.

For a moving storm the most intense inertial current occurs at shallow depths below the mixed layer during and immediately after the passage of the storm (Gill 1984). In this situation the pressure gradient and wave dispersion are not important and continuity alone can cause inertial motion below the mixed layer. This mechanism is particularly important for the generation of inertial oscillations in stratified shallow water. The convergence of currents in the mixed layer gives rise to a vertical displacement at the interface between the mixed layer and the lower layers, which in turn creates a divergence of currents in the lower layers by mass continuity. Such a condition is a consequence of mass conservation and exists independently of the pressure gradient that results from the tilting of the interface and sea surface. Under certain conditions the pressure gradient terms in the momentum equations of the lower layer become very small relative to the other terms. The horizontal currents, however, do not vanish as long as the convergence is nonzero (if the convergence is zero the lower layers are motionless). For baroclinic inertial motion driven by a moving storm the pressure gradient terms become negligible if the speed of the storm is greater than the maximum phase speed of baroclinic inertio–gravity waves. In modeling the inertial currents we can thus drop the pressure gradient terms in the momentum equations and are left with a one-dimensional problem.

Another way to understand storm-generated inertial currents in the lower layer is to consider the reference frame of an observer moving with the storm. For a wind field without a coherent spatial structure, a disturbance caused by the wind stress will propagate away from the area at the speed of baroclinic inertio–gravity waves via pressure gradients. These gradients can be transmitted to the lower layer to generate current there. For a moving storm the disturbance is confined to one side of the observer because the storm is moving faster than the speed of the disturbance. The ocean below the leading edge of the storm is thus seen by the observer as a vertical wall beyond which there is no inertial motion. The current in the mixed layer generated by direct wind forcing is forced to move vertically along the wall by the requirement of mass continuity, a mechanism familiar from coastal upwelling. The continuity constraint thus generates a current in the lower layer. The effect of pressure gradients created during this process is small in comparison with that of mass continuity except at great depths or long after the storm is passed when wave dispersion becomes the dominant mechanism for energy propagation.

The mathematical formulation of the idea described in the previous paragraphs is given in section 2. Greatbatch (1984) derived a set of equations similar to those in section 2, but in a reference frame moving with the storm.

Vertical displacement of the sea surface caused by storms can also produce convergence and pressure gradient. But because the speed of a storm is usually smaller than the maximum phase speed of barotropic inertio–gravity waves, the pressure gradient terms cannot be neglected in the barotropic momentum equations (Greatbatch 1984). Under the assumption of a steadily moving storm or front (in the reference frame moving with the storm), the barotropic response is nonoscillatory (Geisler 1970; Kundu and Thomson 1985). Thus, no barotropic inertial wave is generated. In our data analysis we shall invoke the assumption of a steadily moving wind field whenever a localized intense storm with a well-defined track is identified.

To summarize the discussions of the previous paragraphs the oceanic response to a well-defined intense storm in the inertial frequency band is the generation of baroclinic inertial currents in and below the mixed layer. The pressure gradient terms in the momentum equations can be neglected and, thus, the current time series can be computed from a one-dimensional model by time integration of the forcing at the observation point. The only other situation in which a one-dimensional model is valid would be where the wind field has a spatial scale greater than the barotropic deformation radius (Pollard and Millard 1970). For all other time–space structures of the wind field both baroclinic and barotropic inertial motions can be generated, but realistic simulation of observations is not straightforward. In section 2 we will show that Pollard and Millard's equations can be rederived within the theoretical framework we use in this paper, i.e., in terms of vertical modes.

Section 3 describes the Grand Bank field program and the dataset. In section 4 we use the 170-day dataset to test our one-dimensional simulation model. We will divide the data into two periods according to the wind field patterns. During the first 150 days there were no distinctive and localized storms. In the second period, the last 20 days, three intense storms in succession passed the current meter array. We shall show that in the second period our model gives results in good agreement with the observations both in and below the mixed layer. In the first period, with no well-defined moving storm, the agreement is poor. In section 5 we use the continuity equation to show that horizontal wavenumber, inertial current, and vertical displacement are related. An estimate of the wavelength is made from the current meter and thermistor chain data, and compared to the theoretical value. Section 6 summarizes the fundamental results of this study.

2. Theoretical framework

In this section we shall develop a model suitable for numerical simulation using observed winds. We as-

sume an infinite stratified ocean, with a flat bottom, forced by a wind stress. The equations of motion are given by

$$\frac{\partial u}{\partial t} - fv = -\frac{1}{\rho_*}\frac{\partial p}{\partial x} + \frac{F^x}{\rho_* h} \tag{1}$$

$$\frac{\partial v}{\partial t} + fu = -\frac{1}{\rho_*}\frac{\partial p}{\partial y} + \frac{F^y}{\rho_* h} \tag{2}$$

$$\frac{\partial u}{\partial x} + \frac{\partial v}{\partial y} + \frac{\partial w}{\partial z} = 0 \tag{3}$$

$$\frac{\partial \rho}{\partial t} - \frac{\rho_*}{g} wN^2 = 0 \tag{4}$$

$$\frac{\partial p}{\partial z} + g\rho = 0 \tag{5}$$

where the x-axis is along the storm track, ρ_* and ρ are the mean and perturbation density respectively, N is the Brunt–Väisälä frequency, (F^x, F^y) is a body force distributed within the mixed layer of thickness h, which satisfies

$$\int_{-h}^{0} (F^x, F^y)dz = h(\tau^x, \tau^y) \tag{6}$$

where τ^x and τ^y are the x- and y-component of the wind stress. We can write u, v and p as the sum of a baroclinic and a depth independent barotropic mode:

$$u(z) = u'(z) + U \tag{7}$$

$$v(z) = v'(z) + V \tag{8}$$

$$p(z) = p'(z) + P + g\rho_*\zeta \tag{9}$$

$$\int_{-H}^{0} \mathbf{u}'(z)dz = 0 \tag{10}$$

$$\int_{-H}^{0} p'(z)dz = 0 \tag{11}$$

where ζ is the surface elevation. After vertical integration of (1) to (5) and some algebra we can decouple the barotropic and the baroclinic modes and obtain two sets of equations:

$$\frac{\partial U}{\partial t} - fV = -g\frac{\partial \zeta}{\partial x} + \frac{\tau^x}{\rho_* H} \tag{12}$$

$$\frac{\partial V}{\partial t} + fU = -g\frac{\partial \zeta}{\partial y} + \frac{\tau^y}{\rho_* H} \tag{13}$$

$$\frac{\partial U}{\partial x} + \frac{\partial V}{\partial y} + \frac{1}{H}\frac{\partial \zeta}{\partial t} = 0 \tag{14}$$

$$\frac{\partial u'}{\partial t} - fv' = -\frac{1}{\rho_*}\frac{\partial p'}{\partial x} + \frac{G^x}{\rho_* h} \tag{15}$$

$$\frac{\partial v'}{\partial t} + fu' = \frac{-1}{\rho_*}\frac{\partial p'}{\partial y} + \frac{G^y}{\rho_* h} \tag{16}$$

$$\frac{\partial u'}{\partial x} + \frac{\partial v'}{\partial y} + \frac{\partial w}{\partial z} = 0 \tag{17}$$

$$\frac{\partial^2 p'}{\partial z \partial t} + \rho_* N^2 w = 0 \tag{18}$$

where H is the water depth and

$$G(z) = (G^x, G^y) = \begin{cases} F(z) - \dfrac{h}{H}\tau, & 0 > z > -h \\ -\dfrac{h}{H}\tau, & -h > z > -H. \end{cases} \tag{19}$$

In deriving the barotropic momentum equations we have neglected terms of order η/H where η is the displacement in the interior.

The model response to a moving storm depends on the phase speeds of the inertio-gravity waves, C_n ($n = 0$ barotropic, $n > 0$ baroclinic) and the translation speed of the storm, U_s. Inertial waves can be generated only for $U_s > C_n$. For $U_s < C_n$, the oceanic response is nonoscillatory (Geisler 1970; Kundu and Thomson 1985). The storms we study have translation speeds (5–10 m s^{-1}) much smaller than the barotropic gravity speed ($(gH)^{1/2} \sim 30$ m s^{-1}) and much greater than the baroclinic gravity speeds (≤ 1 m s^{-1}). Consequently, only baroclinic inertial waves are generated. The barotropic response is a nonoscillatory current having a horizontal scale of the external deformation radius, which is approximately 300 km for a water depth of 90 m. In a real ocean the system can deviate from a steady state because of the changing form of storms and a nonuniform translation velocity. In this paper we shall focus on a period in which well-defined storms moved at steady speeds, during which the inertial motion is expected to be predominantly baroclinic.

For a general wind field (where we refer to wind structure that is not in the form of a steadily moving cyclone), both barotropic and baroclinic inertial waves can be generated. The contribution from each mode will depend on the horizontal scale of the wind field. From the dispersion relation of inertio-gravity waves

$$\omega = f(1 + \lambda^2 k^2)^{1/2} \tag{20}$$

where λ is the external or internal deformation radius and k is horizontal wavenumber. We can see that, if the wind scale is much smaller than the external deformation radius, then only baroclinic inertial waves are generated. If the scale of the general wind field is greater than the barotropic deformation radius, then both baroclinic and barotropic modes are possible.

The variables in the baroclinic equations (15)–(18) can be decomposed into vertical modes (Gill 1984).

$$(u', v', p') = \sum (u_n, v_n, p_n)\Phi_n(z) \tag{21}$$

$$\zeta = \sum \zeta_n \Psi_n(z) \tag{22}$$

where the displacement ζ is defined by

$$w = \frac{\partial \zeta}{\partial t} \tag{23}$$

and the summation is from 1 to ∞ (baroclinic modes only). The equations for mode n are

$$\underset{\text{(A)}}{\frac{\partial u_n}{\partial t}} - \underset{\text{(B)}}{fv_n} = -\frac{1}{\rho_*}\frac{\partial p_n}{\partial x} + \frac{G_n^x}{\partial_* h} \tag{24}$$

$$\underset{\text{(C)}}{\frac{\partial v_n}{\partial t}} + \underset{\text{(B)}}{fu_n} = -\frac{1}{\rho_*}\frac{\partial p_n}{\partial y} + \frac{G_n^y}{\rho_* h} \tag{25}$$

$$\underset{\text{(D)}}{\frac{\partial u_n}{\partial x}} + \underset{\text{(E)}}{\frac{\partial v_n}{\partial y}} + \underset{\text{(F)}}{\frac{1}{\rho_* C_n^2}\frac{\partial p_n}{\partial t}} = 0 \tag{26}$$

and $\Phi_n(z)$ and $\Psi_n(z)$ satisfy

$$\frac{d\Psi_n}{dz} = \frac{g}{C_n^2}\Phi_n \tag{27}$$

$$\frac{d\Phi_n}{dz} = \frac{-N}{g}\Psi_n; \tag{28}$$

G_n^x and G_n^y are the source terms given by

$$(G_n^x, G_n^y) = \frac{\int_{-H}^{0} \Phi_n(G^x, G^y)dz}{\int_{-H}^{0} \phi_n^2 dz}. \tag{29}$$

The phase speed of the eigenmode C_n is determined from (27) and (28) or

$$\frac{d^2\Psi_n}{dz^2} + \frac{N^2}{C_n^2}\Psi_n = 0 \tag{30}$$

subject to the boundary conditions $\Psi_n = 0$ for $z = 0, -H$.

The density profile in the study area (see section 3) was put into Eq. (30), which was solved for the eigenvalues C_n. For the first three modes C_n = 0.50, 0.17 and 0.10 m s^{-1}.

For storms moving at 5–10 m s^{-1}, $U_s > C_n$ for all the baroclinic modes. The $\partial/\partial t$ and $\partial/\partial x$ terms in (24)–(26) are related by U_s. The relative magnitudes of the terms in the momentum and continuity equations are (where the letters (A)–(F) refer to the terms in (24)–(26))

$$\text{(A)} : \text{(B)} : \text{(C)} = 1 : \frac{C_n^2}{U_s^2} : \frac{C_n^2 U_s}{U_s^2 fL} \tag{31}$$

$$\text{(D)} : \text{(E)} : \text{(F)} = 1 : \frac{U_s}{fL} : 1 \tag{32}$$

where L is the dimension of the storm. For the Grand Bank storms studied here, U_s = 5–10 m s^{-1}, L = 500–1000 km and thus $U_s/fL \sim 0.05$–0.2 while $(C_n/U_s)^2 \sim 0.0025$–0.01 (for $n = 1$). Consequently, for a first-order estimate of the inertial currents the pressure gradient terms in the momentum equations and the cross track derivative term in the continuity equation can be neglected, though ignoring the cross-track term is less well justified. Under these approximations the currents and displacement can be computed by summing over all the baroclinic modes. The result is simply the original baroclinic equations, (15)–(17), without the pressure gradient terms

$$\frac{\partial u'}{\partial t} - fv' = \frac{G^x}{\rho_* h} \tag{33}$$

$$\frac{\partial v'}{\partial t} + fu' = \frac{G^y}{\rho_* h} \tag{34}$$

$$\frac{\partial u'}{\partial x} + \frac{\partial w}{\partial z} = 0, \tag{35}$$

if we assume the stress is distributed uniformly in the mixed layer

$$G(z) = \begin{cases} (1 - h/H)\tau, & 0 > z > -h \\ \dfrac{-h}{H}\tau, & -h > z > -H. \end{cases} \tag{36}$$

Under the condition $[C_n/U_s]^2 < 1$, no barotropic inertial current is generated as discussed earlier

$$U = V = 0 \quad \text{(in the inertial frequency band)}. \tag{37}$$

We note that outside the inertial frequency band barotropic currents of significant amplitudes can be generated by a steady moving storm. An immediate result of (36) and (37) is that inertial currents in and below the mixed layer are 180° out of phase; a result we shall verify from the data. Equations (33)–(37) are the equations to be used in our data analysis.

The parameter range of the Pollard and Millard model is different from our model. Their model is valid if the scale of the wind field is greater than the barotropic deformation radius. Under this condition, both barotropic and baroclinic inertial currents can be generated. To obtain Pollard and Millard's equations from the modal equations, we sum the barotropic and baroclinic equations (12), (13), (15) and (16) without the pressure gradient terms and use (36). The result is

$$\frac{\partial u}{\partial t} - fv = \frac{\tau^x}{\rho_* h} \tag{38}$$

$$\frac{\partial v}{\partial t} + fu = \frac{\tau^y}{\rho_* h} \tag{39}$$

for the mixed layer, and

$$u = v = 0 \tag{40}$$

below the mixed layer. By a scale analysis we can show that the pressure gradient terms in (12)–(16) are negligible if the scale of the wind field is greater than the barotropic deformation radius, $(gH)^{1/2}/f$. For clarification a comparison of the two models is given in Table 1.

The derivation of Eqs. (33)–(35) involved neglecting friction. In reality the number of modes is limited by friction and only the first few modes contribute. The total current can be obtained by solving the momentum equations (21), (24), (25) and (30) with the pressure gradient terms neglected and a mode number dependent friction added. There is not sufficient vertical resolution in our dataset to warrant modal decomposition, and, hence, the simple inviscid equations (33)–(37) will be used, which can be shown to be equivalent to a two-layer model. The purpose of our analysis in terms of vertical modes is to determine the conditions under which (33)–(37) are valid and the connection between our model and Pollard and Millard's model. We note that in the inviscid model the vertical structure is determined by the stress distribution $F(z)$ and the mixed-layer depth only. The density distribution has no effect on the current profile unless the pressure gradient terms become important, which is the case if $C_n \geq U_s$ or at times several inertial cycles after the passage of the storm at great depths. The situation we analyze in this paper is a succession of storms passing a fixed observation site on the continental shelf. The weak pressure gradient effect from one storm is masked by the forced inertial response of the next storm.

3. Field program and density and current fields

a. Data description

Six months (Apr–Oct 1986) of current meter and thermistor chain data were collected on the northern end of the Grand Bank (de Young and Tang 1988) about 330 km east of Newfoundland (see Fig. 1). An array of three subsurface moorings was deployed with separation distances from 10 km (781–783) to 22 km (782–783). Three guard buoys, large spherical surface floats, were moored in a triangular pattern around each mooring in order to prevent mooring loss to fishing boats. Aanderaa current meters, Aanderaa thermistor chains, and one VACM current meter were used (30 minute sampling). At each mooring site three current meters were deployed, nominally at 20, 30, 60 m (see Table 2 for mooring details). The most shallow instrument (20 m) was deployed on a separate mooring leg to isolate the deeper current meters from wave activity in the surface layer. The surface Aanderaa current meters were equipped with paddle wheel rotors, which reduce the effect of rotor pumping (Hammond et al. 1986). A compass swing (Keenan 1979) was conducted for each current meter both pre and postdeployment. A thermistor chain was placed on each of the deep mooring lines nominally at 30–70 m depth with 5 m vertical spacing. At mooring 781 a second thermistor chain was deployed at the top of the shallow leg to provide 1 m resolution over the 22–32 m depth range.

CTD surveys were conducted at the time of deployment (15–28 April 1986) and recovery (8–21 October 1986) of the current meter moorings. The CTD data were collected with a Guildline Model 8705 digital CTD system. The CTD was used as a vertical sampler with a rosette water sampler attached. CTD calibrations

TABLE 1. Comparison of the Pollard and Millard (1970) model and model used in this paper.

	Pollard and Millard	This work
Wind field	General	Steady moving storm
Condition of validity	$L > (gH)^{1/2}/f$	$(C_n/U_s)^{1/2} < 1$ ($n = 1, 2, \cdots, \infty$, baroclinic)
Barotropic inertial current	Yes	No
Baroclinic inertial current	Yes	Yes
Governing equations	(38)–(40)	(33)–(37)
Inertial current in mixed-layer	Yes	Yes
Inertial current below mixed-layer	No	Yes

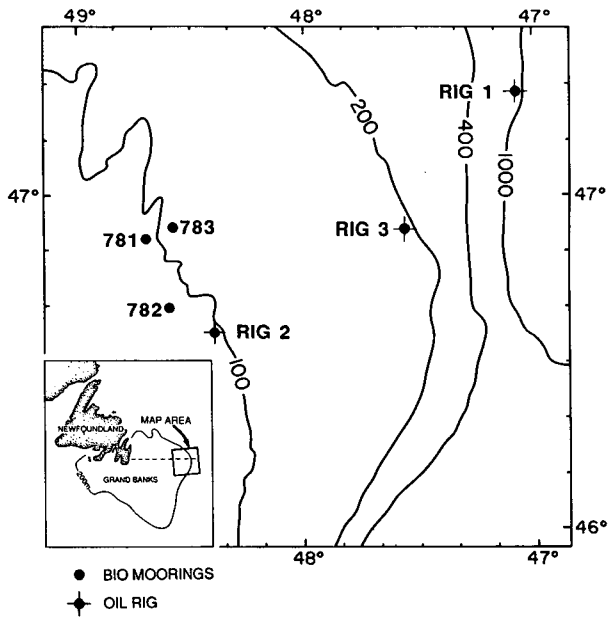

FIG. 1. Area diagram with inset showing geographic location; depths are in meters. Current meter mooring (781, 782, 783) and oil rig (wind measurements) locations are shown. Wind measurements from Rig 1 were used for the period 110–180, Rig 2 days 180–272 and Rig 3 days 272–290. The dashed line in the inset indicates 47°N.

TABLE 2. Current meter and thermistor chain mooring information for *1986* deployments. Partial records are indicated by brackets. Approximate times of complete records are indicated in the last two columns.

Mooring depth (m)	Position	Current meter depths (m)	Thermistor chain depths (m)	Start (h, day)	End (h, day)
781	46°51.54°N	18, 20, 30, (60)	22, 23, 24 . . . 32	18:00	17:00
(90)	48°43.06°W		22, 32, 37, 42 . . . 77	111	286
782	46°40.84°N	20, 30, (60)	21, 26, 31 . . . 77	21:30	21:00
(90)	48°37.56°W			111	286
783	46°53.62°N	24, 34, 64	25, 30, 35, 40 . . . 75	16:30	13:00
(107)	48°35.70°W			112	286

were checked at sea by using reversing thermometers and the collection of water samples, which were analyzed using a Guildline Autosal 8700. The estimated errors in the CTD data are $T \pm 0.01$°C, $S \pm 0.01$ and $\sigma_t \pm 0.01$. For density we will use σ_t unless otherwise noted.

Atmospheric data collected at a nearby oil drilling platform were obtained from the Atmospheric Environment Service. Two oil rigs in the area occupied different positions over the 173 day mooring period. The oil rigs were 40–130 km from the center of the mooring array (see Fig. 1). Data from the nearest rig were used when more than one dataset was available.

b. Density field

The density field on the Grand Bank has a strong seasonal component (Keeley 1981; Drinkwater and Trites 1986). A strong thermocline and associated pycnocline, which exist in summer, are gradually eroded by convective and mechanical mixing. By early winter water on the top of the Bank is nearly vertically homogeneous. Strong horizontal gradients are confined to the shelf edge during this period. Figure 2 shows typical cross-shelf sections of density and temperature along 47°N (see Fig. 1) for August 1986. Cold water is present at the shelf break and in the Avalon Channel next to the coast. Both water masses have been identified as Labrador Current Water (Lazier 1973). Variations in the transport of the Labrador Current have not been clearly established (Thompson et al. 1986) but may be partially responsible for the temporal evolution of the T–S profile (Petrie and Isenor 1985) on the Bank. By early summer a vertical density gradient is present that persists until late fall or early winter. A density profile, the average of 48 CTD casts taken over 24 hours on 10 October 1986, shows a well-developed mixed layer (0–30 m) together with a strong, fairly broad pycnocline (Fig. 3a). The Brunt–Väisälä frequency for this density profile was used to compute the flat-bottomed normal modes for the Grand Bank (Fig. 3b). Normal modes were computed from Eq. (30), which was solved numerically using a shooting method. The zero-crossing for mode 1 is at 48 m, about

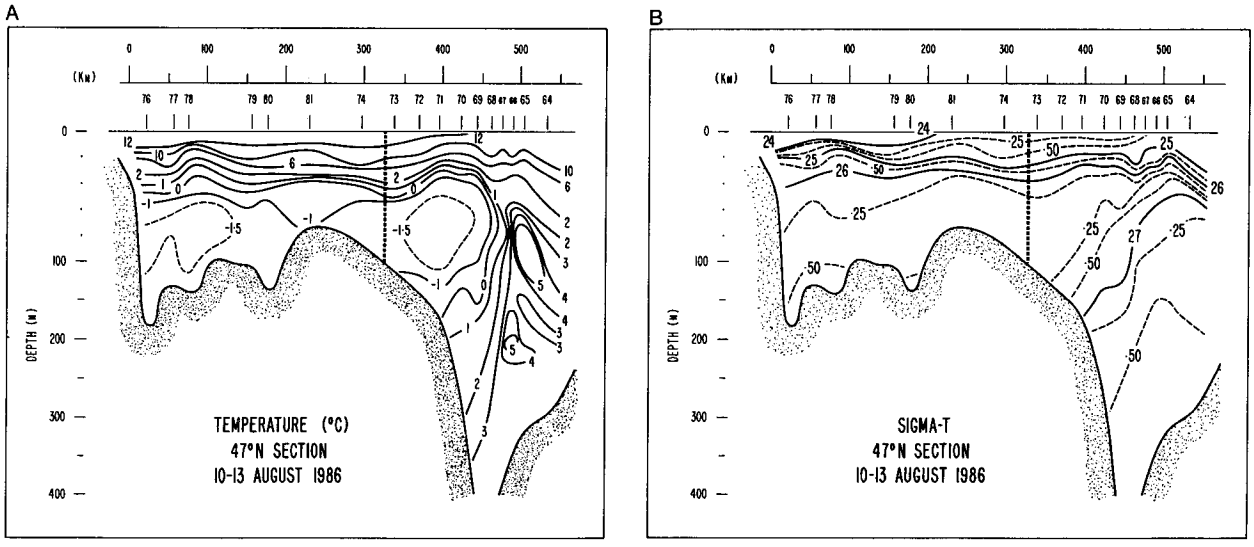

FIG. 2. Transect of (a) temperature and (b) σ_t along 47°N for 10–13 August 1986. The data were provided courtesy of S. Akenhead of the Northwest Atlantic Fisheries Center, St. John's, Newfoundland. The vertical dashed line indicates the mooring site.

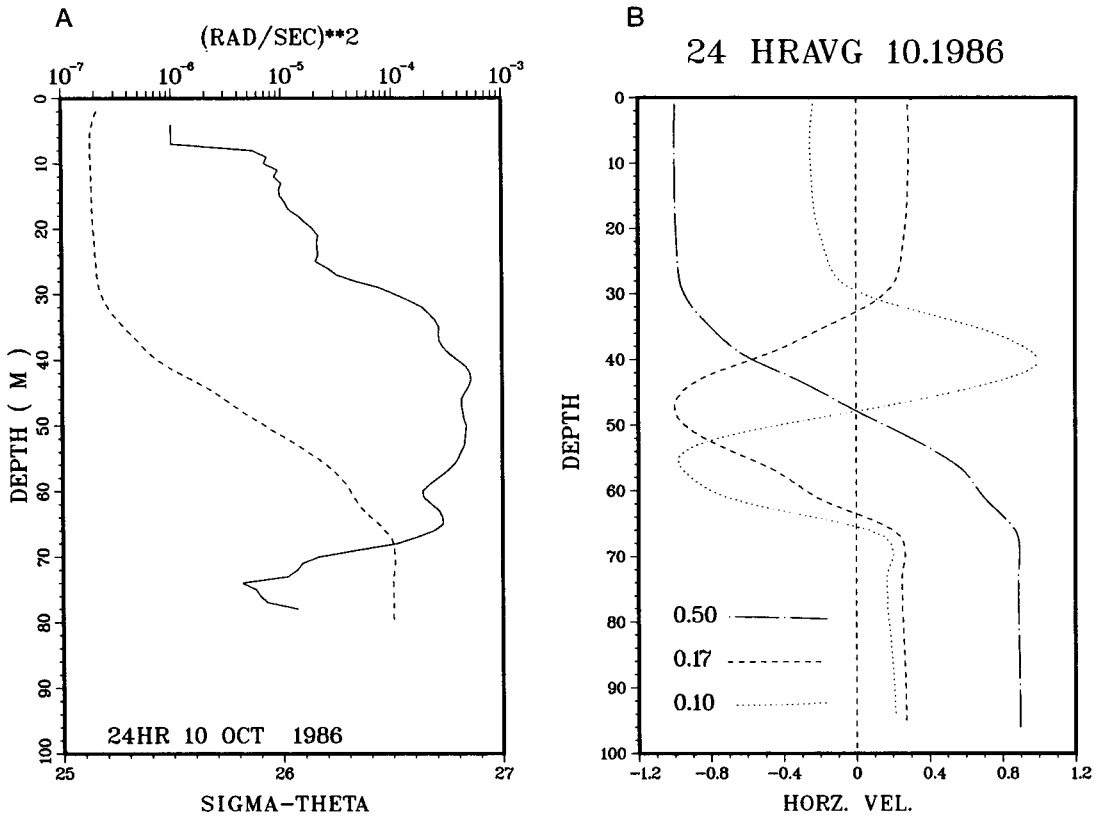

FIG. 3. (a) A 24-hour average (CTD casts every half-hour) of density (dashed line) and N^2 (solid line) taken on 12 October 1986 (day 285). (b) Amplitudes of the first three baroclinic modes computed from the averaged N^2 profile. Phase speeds in m s^{-1} are shown at lower left.

half the water depth (~100 m). The phase speeds (m s^{-1}) for the first three baroclinic modes are given in Fig. 3b.

c. *Observation of inertial currents*

Mean flow on the Grand Bank is weak (<5 cm s^{-1}) and variable from month to month. Much of the mean flow may be associated with residual wind forced motions. A representative kinetic energy autospectrum (Fig. 4) shows four peaks, one broad and three sharp. Two of the peaks are tidal: M_2 (1.94 cpd) semidiurnal and K_1 (1.01 cpd) diurnal; two are wind driven: low frequency (0.2–0.5 cpd) and inertial (1.457 cpd). An estimate of the variance in each frequency band for the first and second half of the record (Table 3) reveals that the inertial band is more energetic than the other bands, representing on average over 50% of the current variance. Because inertial currents are driven by winds, which are intermittent, there will be periods when tidal currents will dominate. The estimates in Table 3 represent long term averages.

Inertial currents rotate clockwise in the Northern Hemisphere. Figure 5 shows the clockwise and counterclockwise components of the spectrum. There is no

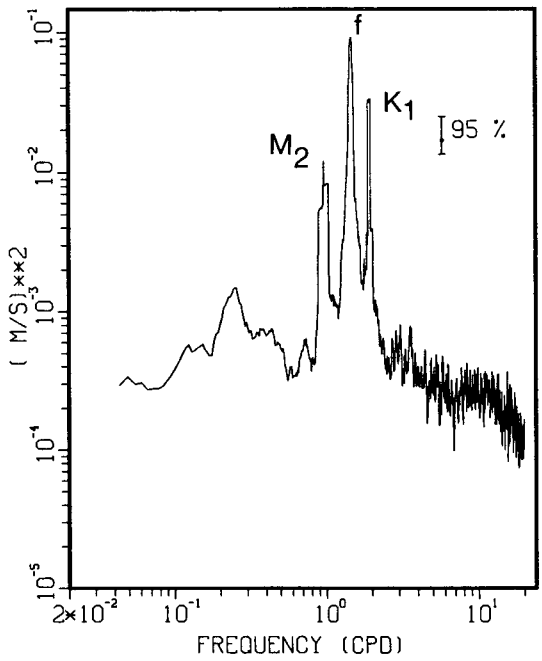

FIG. 4. Kinetic energy autospectrum of currents at site 783, at 24 m depth. The tidal (M_2 and K_1) and inertial peaks are labeled.

TABLE 3. Variance in energy spectrum at different depths for four frequency bands. Estimates ($cm^2 s^{-2}$) are given for the first (111–188) and second half (188–284) of the 174 day records.

		Depth (m)		
Frequency	Period	24	34	64
Low-frequency	1	9.4	8.1	13.1
3–8 days	2	26.4	22.1	29.2
K_1	1	15.8	16.5	28.9
(24 hours)	2	17.6	16.8	16.8
f	1	89.5	41.1	78.9
(16.2 hours)	2	77.9	51.8	73.8
M_2	1	23.2	23.3	40.5
(12.4 hours)	2	31.9	28.3	35.8

detectable inertial peak in the counterclockwise spectrum; all of the inertial energy is in the clockwise component. The inertial peak is at 1.47 cpd with a bandwidth of 0.04 cpd. No departure from the local inertial frequency, 1.457 cpd, can be detected within the statistical uncertainty.

Over the 173 day record a number of strong inertial "events" can be identified. Complex demodulation at the inertial period of the detided current time series yields the time varying amplitude and phase, relative to the start of the record. A demodulation frequency at the local inertial frequency (1.457 cpd) was used with a low pass filter with a cutoff frequency of 0.25 cpd). The u and v components of velocity are 90° out of phase (Fig. 6) with v leading u as expected. The half-width of the inertial current events (Fig. 6a,b) is about 3–5 days, if one assumes that the peaks are symmetric. A comparison of the current response with the wind stress indicates a general correspondence between strong winds and strong inertial currents. There is, however, a lack of quantitative agreement. For example, the strongest and longest period of inertial oscillations occurs from day 180–210 when the wind is relatively weak (Fig. 6c).

The variation of the inertial waves with time can also be obtained by fitting short segments of the data to a sinusoidal wave of the form:

$$u(t) = u_0 \sin(\omega t + \theta) \qquad (41a)$$

$$v(t) = v_0 \cos(\omega t + \theta) \qquad (41b)$$

where u_0, ω and θ are parameters to be determined. The carrier frequency ω is expected to be close to f if inertial oscillations are the dominant mode of motion. We used detided data divided into two-day segments to perform least-square fits. Table 4 shows the fitted ω in three different periods of time when there are strong inertial oscillations. The values of ω vary from 1.433 to 1.489 cpd. The mean error is 1.7%. Since the local value of f, 1.457 cpd, lies within the error limits, a systematic departure from f cannot be determined. The error in the carrier frequency is of a similar magnitude to that determined from the spectral analysis. The term $(u_0^2 + v_0^2)^{1/2}$ as a function of time is plotted in Fig. 7. The curves are very similar to those in Fig. 6.

Cross-spectra of velocity among all the moorings show strong coherence at the inertial frequency. Co-

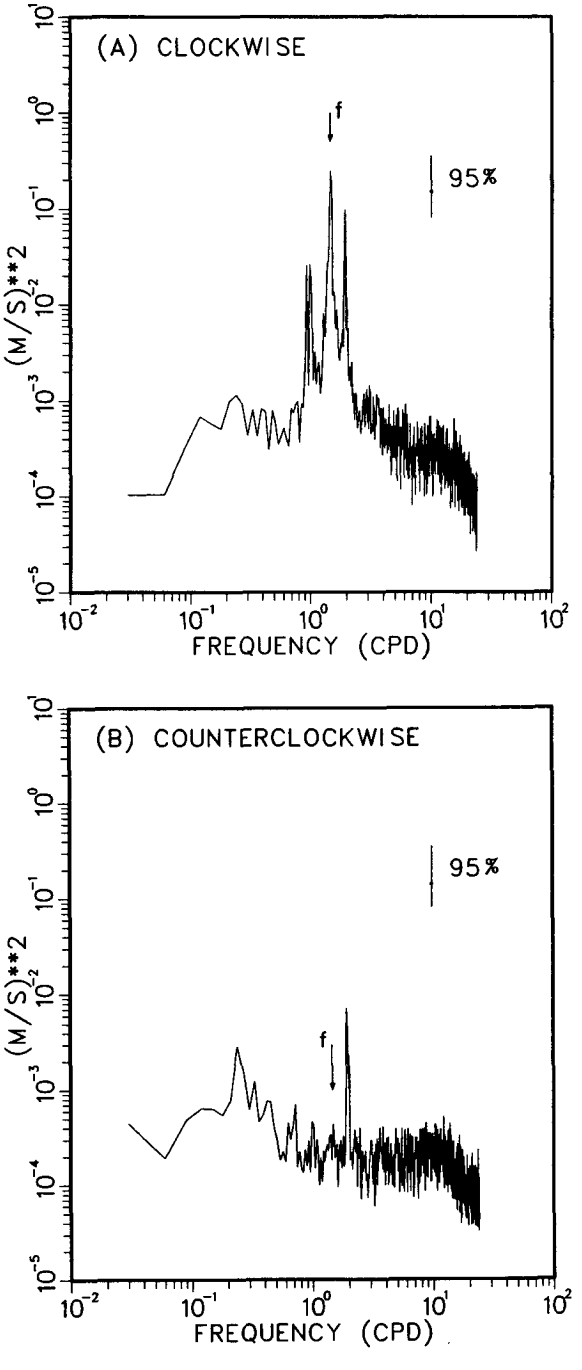

FIG. 5. Rotary spectrum of currents at 783 at 24 m depth: (a) clockwise and (b) counterclockwise. The arrows indicate the position of the local inertial frequency. The error bars are the 95% confidence level at the inertial frequency.

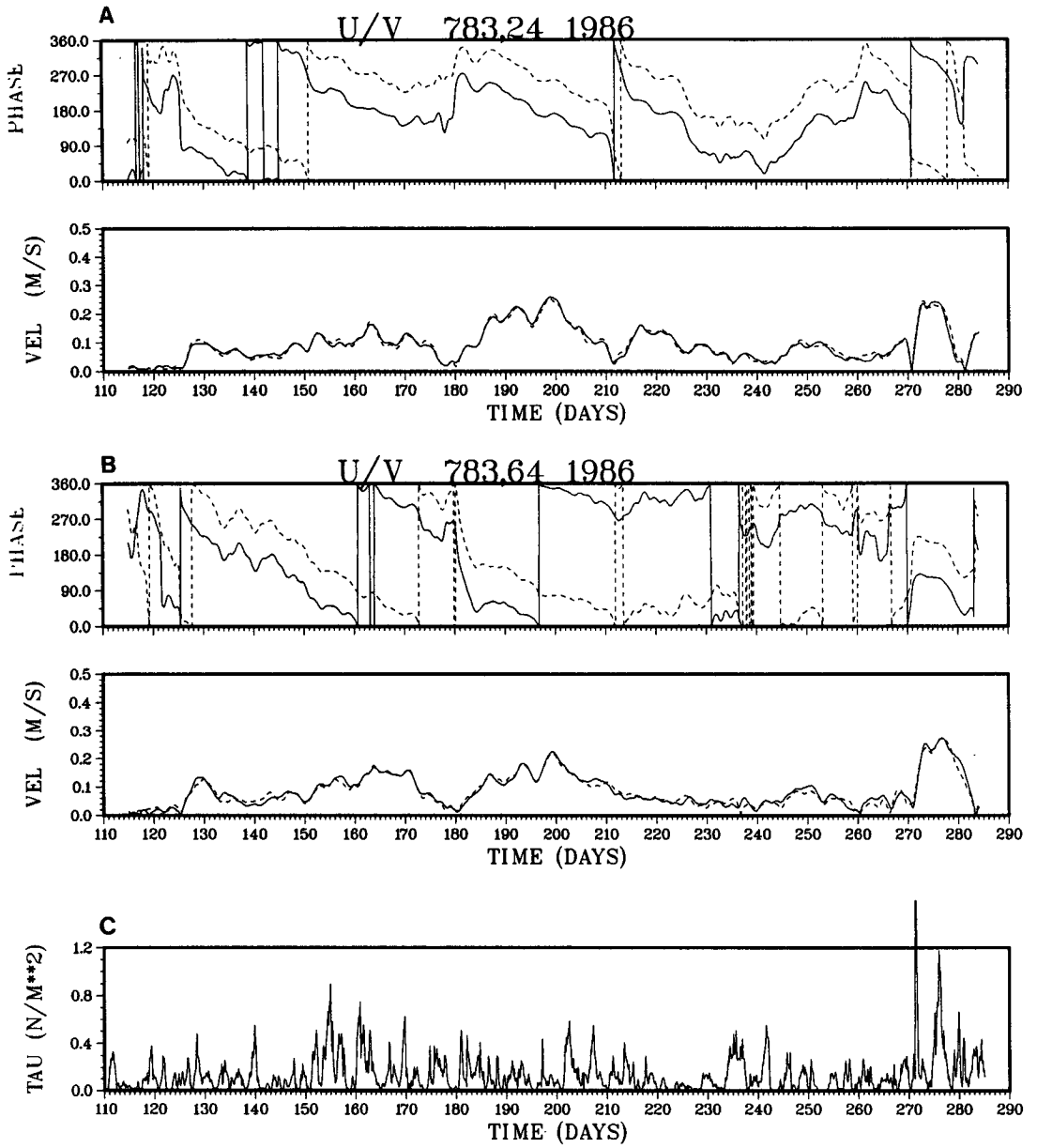

FIG. 6. Complex demodulation of u (solid) and v (dashed) component currents at (a) site 783 at 24 m depth: (b) 783 at 64 m depth. Phase is relative to the start of the record. The demodulation frequency was $f = 1.457$ cpd. The total wind stress computed from the oil rig wind data is shown in (c).

herence-squared between moorings 783 and 782, at 34 and 30 m depth, respectively, is greater than 0.9 at the inertial frequency. It is not possible, however, to detect significant phase propagation within the array at the inertial frequency. Analysis of short sections of the record, when there was strong storm forcing, revealed phase differences of less than 5°, within the error limits (±8°). Cross-spectra in the vertical reveal that, for the last section of the record (day 260–283), the surface and lower layer inertial currents are nearly 180° out of phase. Fitting segments of data using (41a) and (41b) to determine the phase propagation in separate periods was attempted. Unfortunately, the phases obtained by this method are very sensitive to small variations in the frequency. No conclusive results were obtained.

4. Detailed model comparison

The goal of this section is to study the inertial response to two different types of wind forcing (moving storms and "general" winds), and to test the simple model developed in section 2. We will use this model

TABLE 4. Carrier frequency determined from fitting short segments of data (2 days) at site 783 to Eqs. (41a) and (41b). The three periods selected have strong inertial oscillations. The errors are the standard deviations of the fitted frequencies of the segments in the given time periods.

Depth (m)	Frequency (cpd) Days 156–172	Days 194–208	Days 272–280
24	1.458 ± 0.008	1.464 ± 0.017	1.462 ± 0.003
34	1.475 ± 0.027	1.464 ± 0.008	1.489 ± 0.036
64	1.433 ± 0.038	1.464 ± 0.008	1.435 ± 0.079

to simulate the data described in section 3. The current meter data runs from April–October 1986. The strongest wind forcing occurs during the passage of three well-defined storms at the end of the period September–October that overlaps the period of strongest stratification (July–September). In section 4a it will be seen that the model performs well during the end period when the assumptions about storm structure are met. During the rest of the record, however, the simulation does poorly (section 5b).

a. Storm-forced baroclinic inertial currents

Section 2 shows that for a moving storm the inertial oscillation is predominantly baroclinic. The pressure gradient terms in the momentum equations can be neglected and the inertial currents can be simulated by solving numerically the one-dimensional equations (33) and (34).

From the 170 day observation period we selected 20 days (265–285) during which three intense storms passed the mooring site in succession. The three storms moved at speeds of 5–10 m s^{-1} in a roughly northeasterly direction (Fig. 8). These storms are about 800 km in diameter with embedded complexity such as fronts which we shall ignore because of a lack of data. The other periods with large inertial currents (e.g., days 150–170, 185–210) have strong winds but there were no well-defined storms present.

In order to isolate the inertial frequency response, tidal analysis and filtering were carried out on the current time series. After harmonic analysis (Godin 1972) on 29-day sections of the record, the major tidal constituents were removed. The detided records were then high-pass filtered with a filter whose cutoff was at 32 hours. This filtering removed less than 0.1% of the inertial energy. The wind and inertial current time series from two depths for the last 20 days of the record are shown in Fig. 9. Inertial oscillations are weak and variable for the first six days of the current records. A strong inertial response is associated with each of the three strong storms during the period, days 271, 275 and 279 (Fig. 8). The time series plots indicate that the upper and lower layer inertial currents are approximately 180° out of phase.

A more detailed view of the vertical structure can be obtained by fitting the current data at different depths in a 3-day interval using (41a) and (41b), and using the local inertial frequency for ω. Figure 10 shows $(u_0^2 + v_0^2)^{1/2}$ and θ relative to that of the top current meter at five depths for two periods, days 272–275 and 275–278. The currents are almost independent of depth in the mixed layer. The lower layer current has an opposite direction to the mixed-layer currents. Because there is only one current meter below 50 m, the vertical structure cannot be resolved further. The structure in Fig. 10 indicates that the assumption of a two-layer current is a reasonable approximation for these periods.

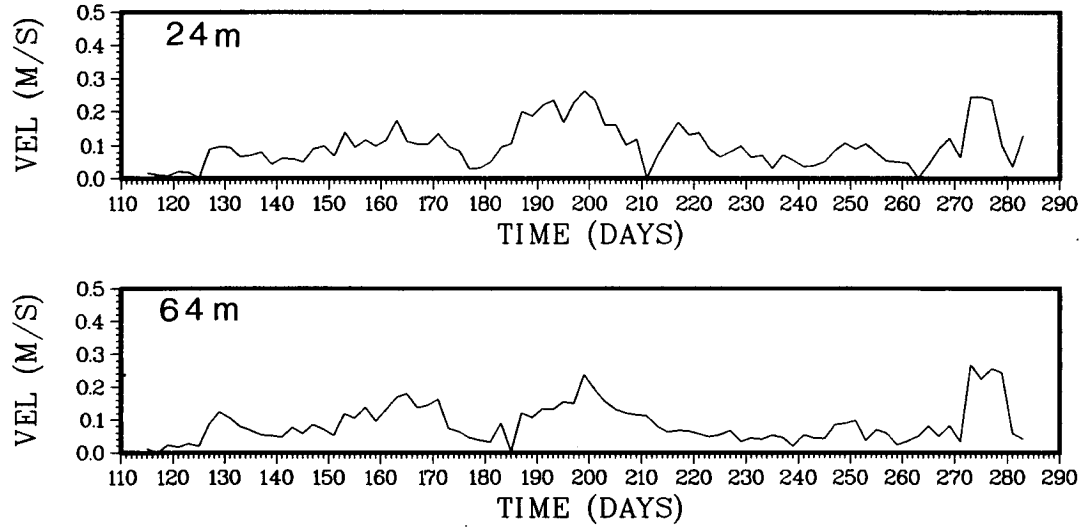

FIG. 7. Magnitude of inertial oscillations determined from fitting short segments of the data (2 days) at site 783 to Eqs. (41a, b). The upper and lower panels are results for 24 m and 64 m depth respectively.

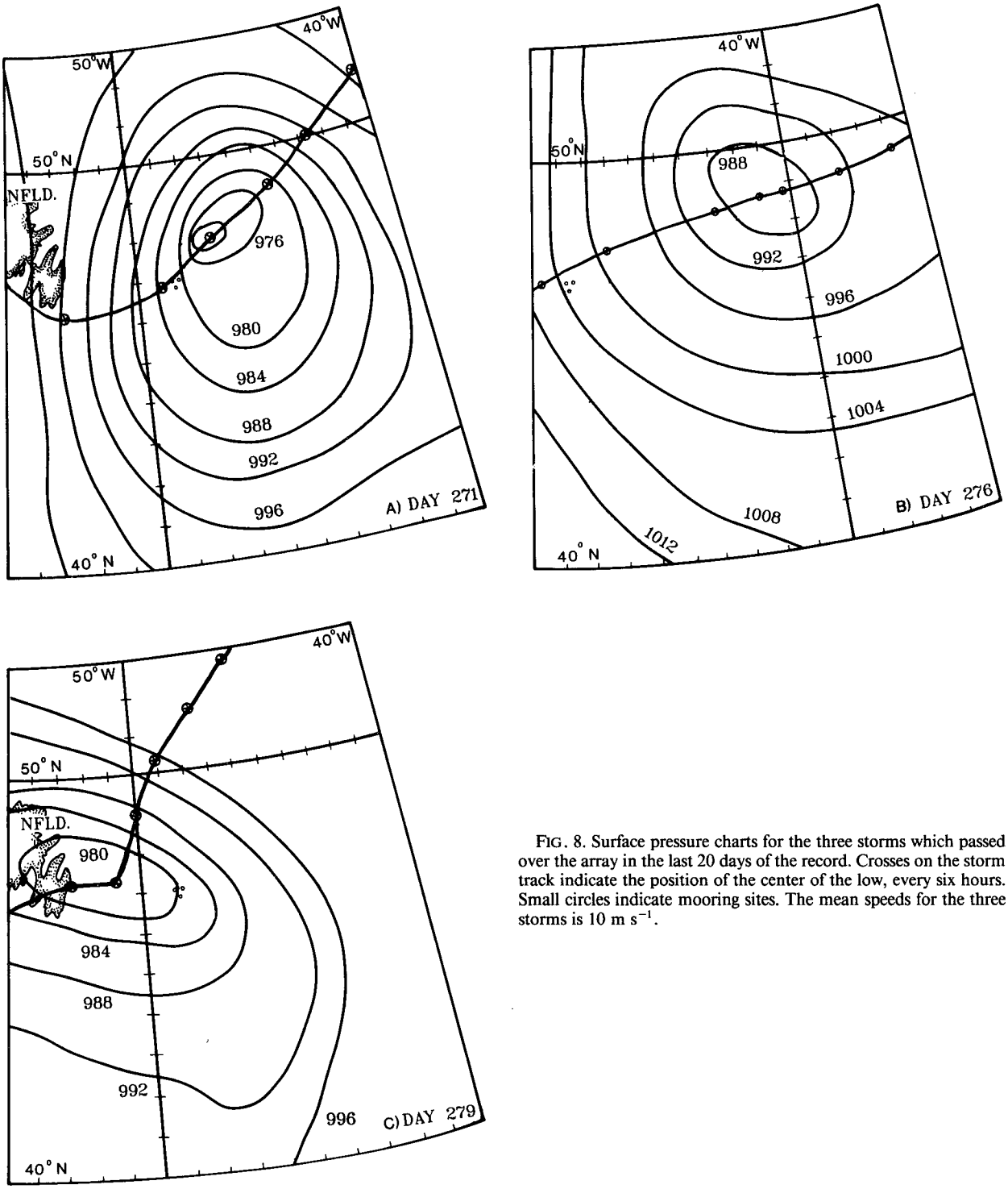

FIG. 8. Surface pressure charts for the three storms which passed over the array in the last 20 days of the record. Crosses on the storm track indicate the position of the center of the low, every six hours. Small circles indicate mooring sites. The mean speeds for the three storms is 10 m s^{-1}.

Equations (41a) and (41b) are also used to find the phase differences among the three moorings during the storms. The phases in each layer agree to within 25°, and there is no systematic difference from one mooring to another. This suggests that the coherent scale is at least 25 km (the largest separation between the moorings). Linear theory (Geisler 1970; Kundu and Thomson 1985) predicts that the inertial wave in the wake of a moving storm has a wavelength of $2\pi U_s/f$, which is 300–600 km for U_s = 5–10 m s^{-1}. Our observation

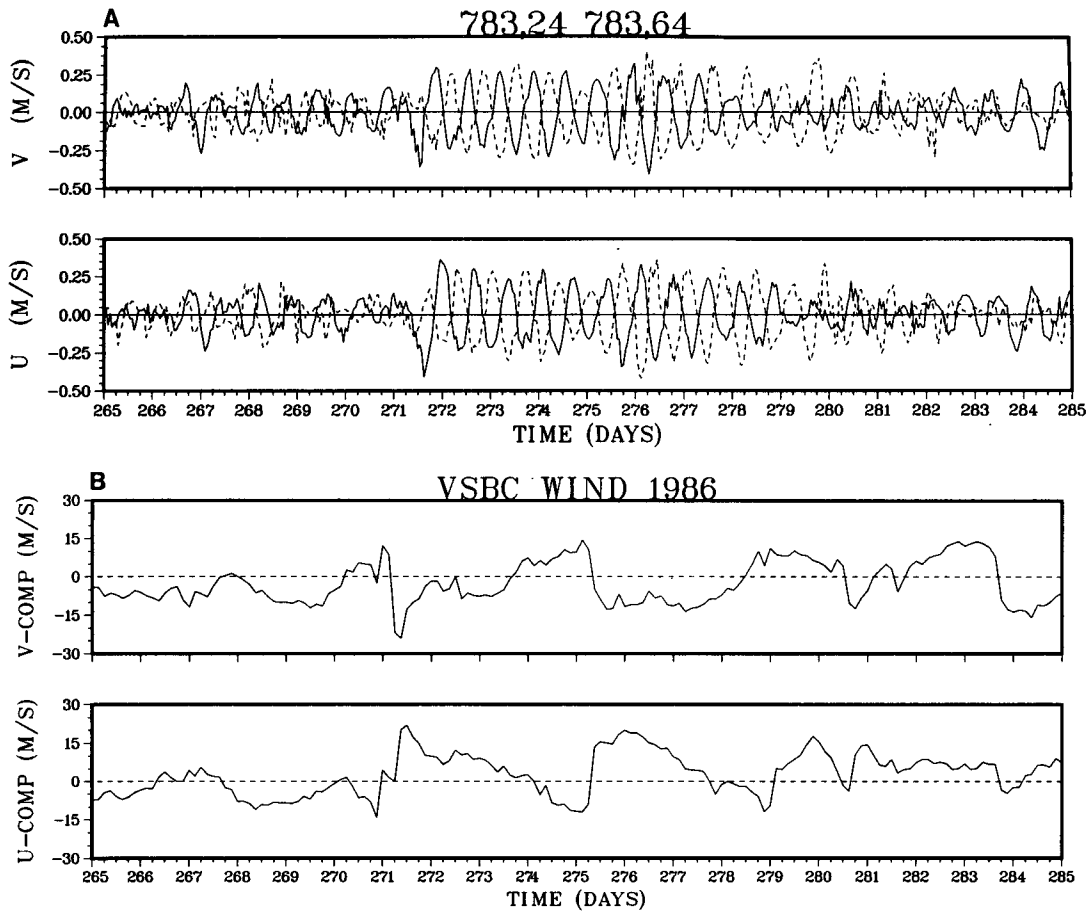

FIG. 9. Time series of (a) u and v currents with the tide removed, and high-pass (cutoff at 32 hours) filtered. Both the upper layer (solid) and the lower layer response are shown. The wind velocity components as measured at a nearby oil rig (see Fig. 1) are shown in (b).

is consistent with the theory, although the wavelength cannot be determined from the data directly (see section 6 for further discussion of wavelength).

Model simulations were carried out using (33) and (34) in finite difference form using a centered difference scheme with the first step forward differenced. The wind time series shown in Fig. 9 provided the forcing. The winds, which were measured at 75 m height, were multiplied by 0.9 to give wind speed at 10 m (Smith 1981; de Young and Tang 1989). Wind stress was computed using the formula of Large and Pond (1981). The mixed layer depth, which increased during the period because of cooling and mechanical mixing driven by strong winds, was determined from temperature profiles (Fig. 11). Linear friction was used, consistent with the modal separation, with a spindown time of four days. The spindown time was chosen based on the observed decay time scale (Fig. 6). A summary of the model parameters is given in Table 5.

The hindcast for the last 20 days of the record does reasonably well for both amplitude and phase (Fig. 12) during the three storms (day 271–280). The upper layer

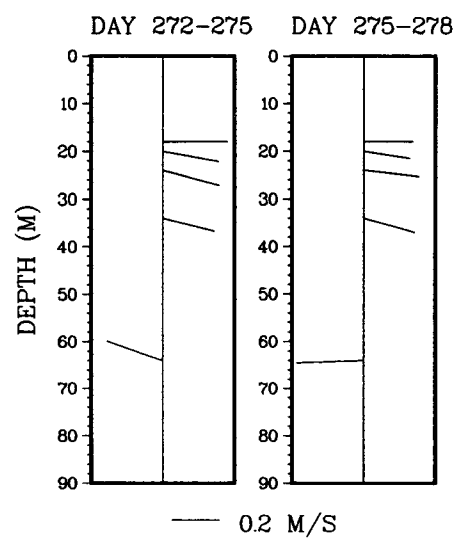

FIG. 10. Magnitude and relative phase of inertial waves at depths 18, 20, 24, 34, and 64 m. Data for 24, 34, and 64 m are from Station 783. Data for 18 and 20 m are from Station 781. The phase is measured counterclockwise from the horizontal direction.

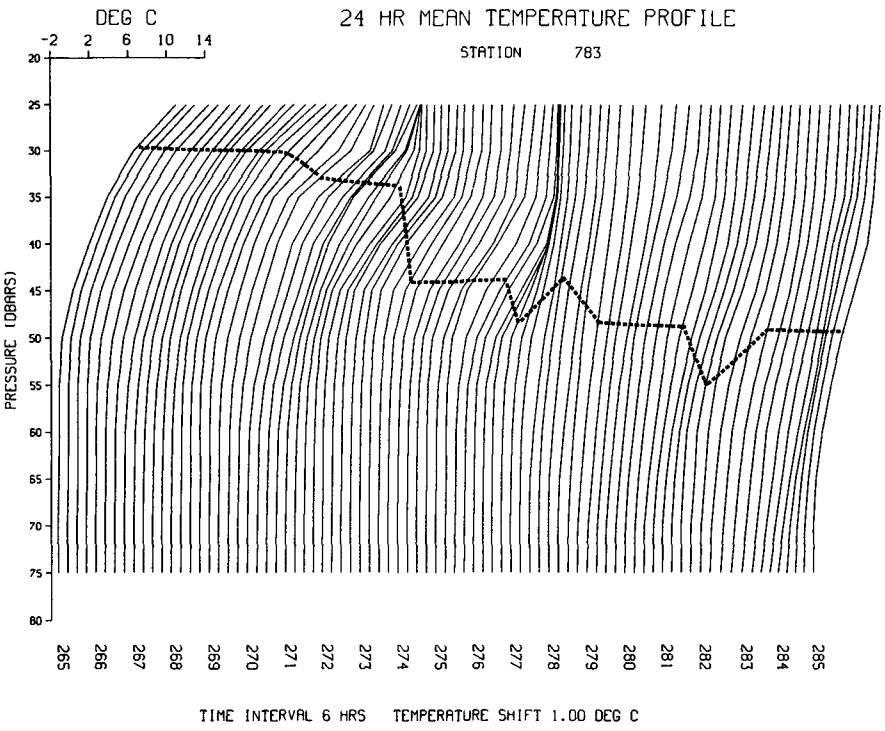

FIG. 11. The temperature profile as determined from the thermistor chain data. Each line represents a 24 hour average. The dashed line indicates the bottom of the mixed layer as determined from the maximum in dT/dz. Note that the mixed layer depth increases from day 270 onward reaching a maximum on day 281.

response is somewhat overestimated while the lower layer response is somewhat underestimated. Fine-tuning of the model by varying the mixed layer depth, the wind reduction factor, and the spindown time could improve the model fit. Some attempt was made at this, however, it was not clear how to constrain the various parameters. The model results presented here are based on reasonable estimates of the model parameters. We note that the currents generated by the third storm (day 279) have a higher amplitude in the lower layer than in the upper layer (Fig. 9), and the model results are poor. This could be due to the fact that the third storm changed direction in its course (Fig. 8) and the condition for steadily moving, fixed storm characteristics is not met.

A close inspection of Fig. 9 reveals that there is an 18–24 hour delay in the development of inertial currents in the lower layer during the first and second storm (day 271 and 276). This delay is not reproduced in the model results. A possible explanation is that following the arrival of the storms a forced nonoscillatory barotropic current of short duration ($<\frac{1}{2}$ day) is rapidly generated (since $U_s < C_0$), which is not completely filtered out by the high-pass filter (cutoff period is 32 hours). This short barotropic pulse is disguised as an inertial wave and partially cancels the lower layer inertial oscillation. There is, however, no simple way to simulate the barotropic current within the framework of the one-dimensional model. We note that this delay is not related to vertical propagation frequently observed in the deep ocean, which is a result of the pressure gradient effect. The lower layer current we observe here is primarily a consequence of mass continuity.

b. *Overall model comparison*

Detailed comparisons were run for many different periods of the records. Rather than present all of these comparisons individually we will discuss the complex demodulation of the model velocity for the whole period. For this comparison a fixed mixed-layer depth of 25 m was used for the period 110–265 because there is no thermistor chain above this depth. For days 265–285 the deepening mixed-layer depth based on temperature data was used. Wind data for the period 110–180 was from Rig 1, 180–272 from Rig 2, and for the period 272–290 wind data from Rig 3 was used (see

TABLE 5. Hindcast model parameters.

H	water depth—107 m
H_{mx}	mixed layer depth—maximum of dT/dz
$\rho 1$	upper layer density 1025 (kg m^{-3})
$\rho 2$	lower layer density 1026 (kg m^{-3})
f	1.06×10^4 s^{-1}
Spindown time	4 days
Δt	time step—360 seconds

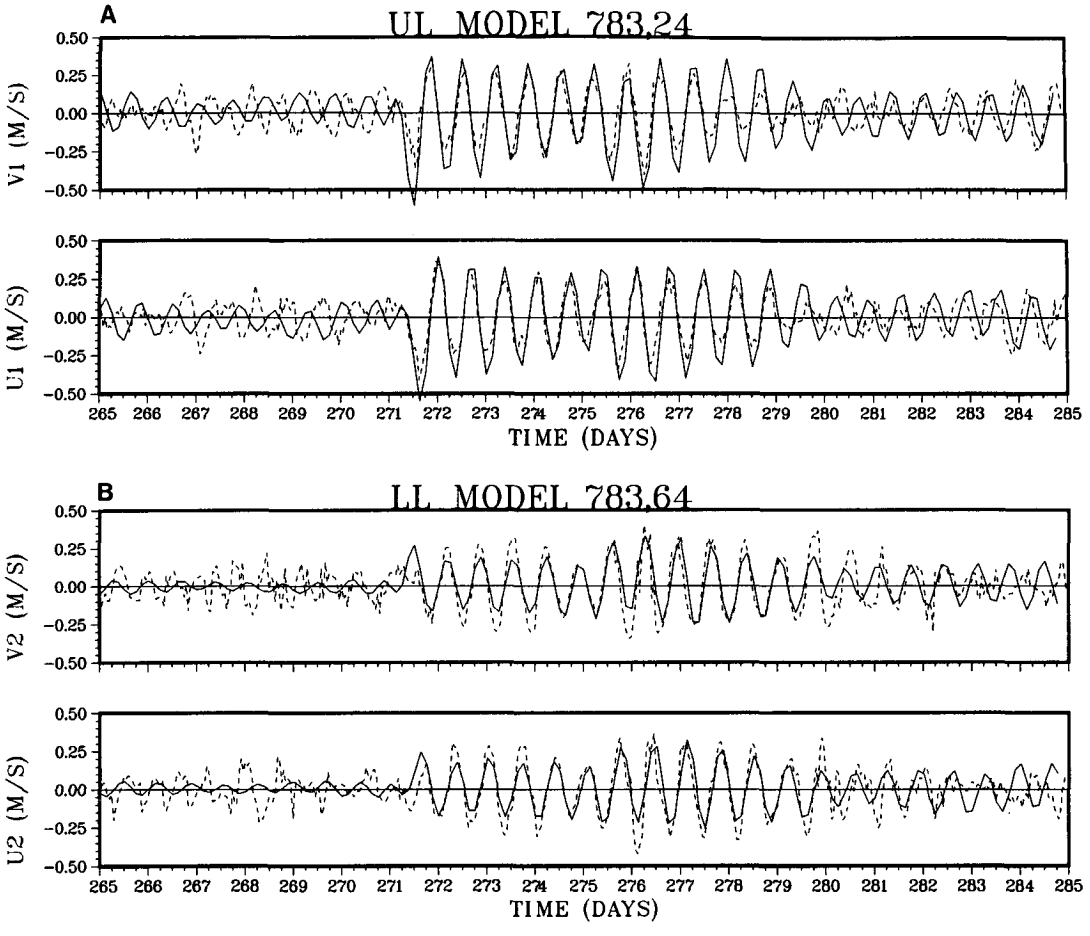

FIG. 12. Hindcast simulations (solid line) and observed detided currents (dashed line) for the last 20 days of the record. For the (a) upper layer, observed current at 24 m is used; for the (b) lower layer, observed current at 64 m is used.

Fig. 1). All other model parameters are the same as those for the detailed simulation shown in Fig. 12 (see Table 5). Since the wind scales are much greater than the distances between the mooring and the rig sites, the errors associated with the different rig positions are negligible.

Figure 13 shows the model hindcast for the upper and lower layers together with the complex demodulation of the observed currents at 24 and 64 m depth. There are a number of periods (110–130, 150–160, 180–190) when the hindcast upper layer response is too large. There are also a number of periods (160–170, 195–210) when the upper layer response is reasonably well predicted, however, the lower layer response is greatly underpredicted. Examination of weather charts for these periods reveals the forcing during these periods to be of large spatial extent. These large scale pressure systems are also observed to move relatively slowly (<5 m s^{-1}). The model does poorly because assumptions about the forcing (scale, translation speed) are not met. In such a case both the barotropic mode and baroclinic modes and the pressure gradient effect should be considered. No simple one-dimensional model can simulate the response. When the model assumptions are met, during fast moving storms (270–280) the hindcast is quite successful in modeling both the amplitude and phase in the upper and lower layers.

To find out whether there is any difference in the frequency response of the inertial currents in the storm-forced period and the other periods we performed a spectral analysis using only data from the early period (days 110–265). The general characteristics and the peak frequency are the same as the spectrum in Fig. 5a.

5. Horizontal scale and vertical displacement

It is generally believed that the horizontal scales of inertial motion are linked to the structure of the forcing wind field and the stratification of the ocean. A large range of horizontal scales have been observed (Pollard

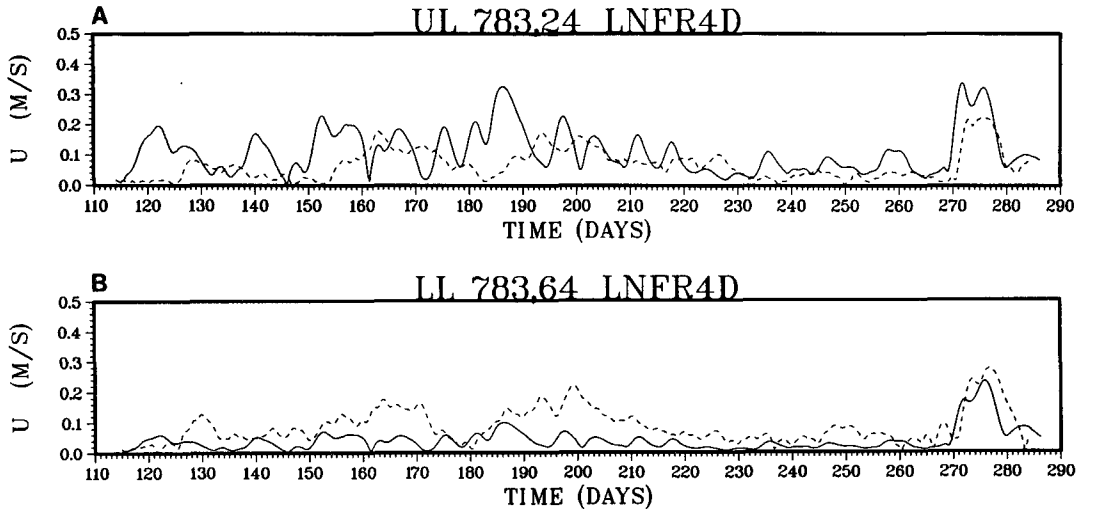

FIG. 13. Complex demodulation of the simulated (solid line) and observed (dashed line) currents for the entire period. The u-component for the upper and lower layer simulation is plotted together with (a) upper (24 m depth) and (b) lower (64 m depth) layer currents.

1980; Kunze 1986; Shay and Elsberry 1987). Dispersive inertial waves and storm-forced inertial waves have different properties, and should be distinguished in the interpretation of data. The wavelength of dispersive inertial waves is given by the dispersion relation (20). Assuming a baroclinic phase velocity of 0.4 m s^{-1} and a barotropic phase velocity of 30 m s^{-1}, and defining inertial motion as inertio–gravity waves with frequency ω/f in the range between 1 and 1.1 we find the barotropic and the baroclinic inertial waves have wavelengths greater than 3000 and 50 km, respectively. For baroclinic inertial oscillations generated by a moving storm, the phase is fixed relative to the position of the storm, and thus, the wavelength is simply $2\pi U_s/f$. The mean speed of the storms in the last 20 days of the study period is estimated to be 8.1 m s^{-1} giving a wavelength of 470 km.

A direct determination of the wavelength from our dataset cannot be made because of the small horizontal separation of the moorings. However, since the horizontal scale is related to the vertical displacement by the continuity equation, we can use the thermistor data to calculate the vertical displacement and the wavelength.

We integrate the continuity equation (17) from the bottom to a depth $-D$ below the mixed layer and obtain

$$\frac{\partial \eta_D}{\partial t} = -(H - D)\frac{\partial u'}{\partial x} \tag{42}$$

where η_D is the vertical displacement at $z = -D$. Replacing $\partial/\partial t$ in (42) by f and $\partial/\partial x$ by horizontal wavenumber, k, we find the magnitude of η_D and u' is related by

$$|\eta_D| = (H - D)k|u'|/f. \tag{43}$$

Given $|\eta_D|$ and $|u'|$, the wavelength can be computed from this equation.

The vertical displacement was calculated from the thermistor chain data using low-pass filtered vertical temperature gradients and high-pass filtered temperature. Figure 14 shows time series plots of displacement and temperature for days 265–285 at 40 m. The data are noisier than the current data, but inertial oscillations of 20 m maximum amplitude can clearly be seen. Considering the assumption of no strain used in the calculation of the displacement and the contamination by the mooring motion, we estimate the error to be about 15%. We note advection can also produce inertial signals in the data if there are significant horizontal temperature gradients. CTD data show there is no shelf scale temperature gradient (Fig. 2). At smaller scales

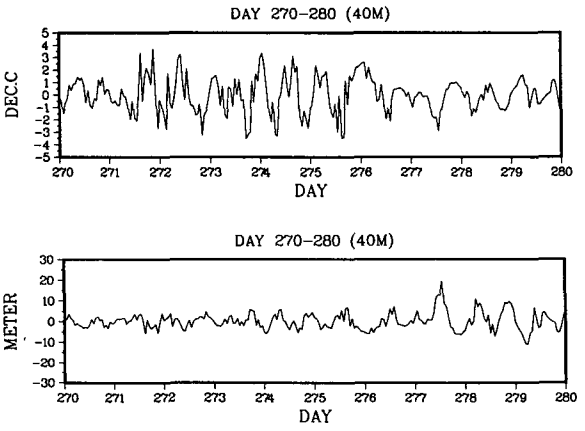

FIG. 14. The displacement and temperature perturbations at 40 m depth as determined from the temperature profile measured by thermistor chains on mooring 783.

temperature variation is of the order 0.5°C/100 km. For a 0.25 m s^{-1} inertial current this temperature gradient results in a peak-to-trough temperature difference of 0.14°C, which is much smaller than the observed temperature fluctuation (Fig. 14). The effect of advection can thus be neglected.

The frequency spectrum of displacement for the entire mooring period (Fig. 15a) shows two distinct peaks corresponding to the inertial oscillation and the M_2 tide. The spectrum for days 270–280 (Fig. 15b) is dominated by the inertial peak. We estimate $|\eta|$ by integrating the spectrum in Fig. 15b over the inertial frequency band and obtain $|\eta| = 2.6$ m. To get the vertical displacement at the same depth as the current meter (64 m) we interpolate the value to 64 m assuming a linear decrease of the displacement to the bottom. The magnitude of u' at 64 m is taken from Fig. 6 as 0.25 m s^{-1}. Equation (43) gives the wavelength of the inertial wave, $\lambda = 2\pi/k = 380$ km, which is within 19% of the theoretical value based on the speed of the storms. Considering the errors and assumptions used in the calculation we conclude that the observation is consistent with the first order linear theory.

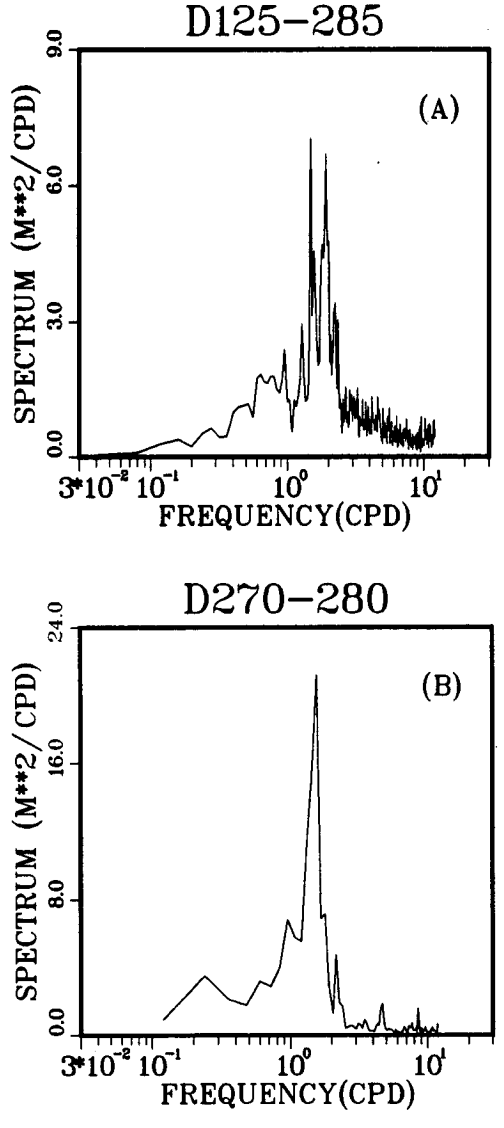

FIG. 15. Frequency spectrum of displacement at 40 m, computed from thermistor chain at mooring 783 for (a) the entire record and (b) the period days 270–280. The computation has 17 degrees of freedom for (a), and 3.2 degrees of freedom for (b).

6. Conclusions and discussion

An analysis of nearly half a year of current data from the northern Grand Bank revealed the presence of strong inertial oscillations. These inertial oscillations had the following properties:

1. account for almost half of the total variance
2. during storms, have roughly equal current amplitudes in the mixed and the lower layers, but are 180° out of phase
3. during periods of strong winds but no identifiable storm, there is no consistent relationship between the winds and the inertial oscillation
4. wavelength derived from the vertical displacement data is consistent with first order linear theory of inertial motion generated by storms.

A simple one-dimensional model was developed to simulate these inertial currents. Scale analysis was applied to show that the pressure gradient terms in the momentum equation can be neglected for the storm-forced inertial wave and no barotropic inertial current is generated since the storms move at speeds slower than the maximum speed of inertio–gravity waves. The inertial currents below the mixed layer are produced as a consequence of mass continuity. The model succeeds in simulating inertial currents in both the upper and lower layers. Earlier in the record when strong winds force inertial oscillations, but no well-defined storm is present, the one-dimensional model cannot adequately describe the dynamics of the system. We suggest that there may be a barotropic inertial current response during these periods together with pressure gradient effects, which are both neglected in the simulation model. Barotropic models have been developed (Chang 1985), however, in general the barotropic response has been found to be small.

In taking the one-dimensional approach there are a number of factors that have been ignored. For example, the influence of the coastal boundary and topography, which have been shown to be important elsewhere (Shay and Elsberry 1987). The generation of a baroclinic wave at the coast that propagates offshore at the internal group velocity [0.5–1 m s^{-1}] has been shown to be important for inertial currents in the Gulf of Lions (Millot and Crépon 1981). On the northeastern edge of the Grand Bank 350 km from shore, this effect was not detected. At the eastern edge of the Grand Bank

there is, however, the possibility of reflection and focusing of inertial currents by the shelf-break current present there, the Labrador Current (Petrie and Isenor 1985). The modification of inertial currents by mean currents, which has been investigated by Kunze (1985), may also play some role in influencing inertial currents on the Grand Banks.

Nonlocal and small scale forcing may also be important. Wind measurements made at a single point, all that was available to us, do not reveal the strength of such effects. An analysis of Seasat scatterometer data by D'Asaro (1987) indicated that the horizontal scales of the inertial currents were set by the advection speed and wind field scales that are smaller than the advective scales U_s/F. D'Asaro suggested that detailed modeling would require wind measurements to scales at least U_s/f.

Acknowledgments. For useful internal reviews and discussion of this work we thank B. Petrie and P. Smith. Support for the project was provided by the Canadian Panel on Energy Research and Development (PERD).

REFERENCES

Chang, S. W., 1985: Deep ocean response to hurricanes as revealed by an ocean model with free surface. Part I: Axisymmetric case. *J. Phys. Oceanogr.*, **15,** 1847–1858.

——, and R. A. Anthes, 1978: Numerical simulations of the ocean's nonlinear baroclinic response to translating hurricanes. *J. Phys. Oceanogr.*, **8,** 468–480.

D'Asaro, E., 1987: Horizontal scales of wind forced inertial motions. *Proc. Hawaiian Winter Workshop: Dynamics of the Oceanic Surface Mixed Layer,* P. Muller, D. Henderson, Eds., Hawaii Institute of Geophysics Special Publication, 159–180.

de Young, B., and C. L. Tang, 1988: Current meter, CTD and meteorological observations on the Northern Grand Banks (47°N, 38°W) for April–October 1986. *Can. Data. Rep. Hydrogr. Ocean Sci.*, **63,** 94 pp.

——, and ——, 1989: An analysis of Fleet Numerical Oceanographic Center winds on the Grand Banks. *Atmos. Ocean,* **2,** 414–427.

Drinkwater, K., and R. W. Trites, 1986: Monthly means of temperature and salinity in the Grand Banks region. *Can. Tech. Rep. Fish. Aquat. Sci.*, **1450,** 111 pp.

Geisler, J. E., 1970: Linear theory of the response of a two-layer ocean to a moving hurricane. *Geophys. Fluid Dyn.*, **1,** 249—272.

Gill, A., 1984: On the behaviour of internal waves in the wakes of storms. *J. Phys. Oceanogr.*, **14,** 1129–1151.

Godin, G., 1972: *The Analysis of Tides.* University of Toronto Press, 264 pp.

Greatbatch, R. J., 1984: On the response of the ocean to a moving storm: Parameters and scales. *J. Phys. Oceanogr.*, **14,** 59–78.

Hammond, T. M., C. P. Pattiaratchi, M. J. Osborne and M. Collins, 1986: Field and flume comparisons of the modified and standard (Savonious-Rotor) Aanderaa self-recording current meters. *Deutsch. Hydrogr. Z.*, **39,** 41–63.

Keeley, J. R., 1981: Mean conditions of potential temperature and salinity along the Flemish Cap section. *Mar. Environ. Data Serv. Tech. Rep.* **9,** 148 pp.

Keenan, P., 1979: Sources of compass error within the Aanderaa recording current meter: Revised 1979. Bedford Institute of Oceanography, Rep. Ser. BI-R-79-6, 70 pp.

Kroll, J., 1975: The propagation of wind-generated inertial oscillations from the surface into the deep ocean. *J. Mar. Res.*, **33,** 15–51.

Kundu, P., and R. E. Thomson, 1985: Inertial oscillations due to a moving front. *J. Phys. Oceanogr.*, **15,** 1076–1084.

Kunze, E., 1985: Near-inertial propagation in geostrophic shear. *J. Phys. Oceanogr.*, **15,** 544–565.

——, 1986: The mean and near-inertial velocity fields in a warm-core ring. *J. Phys. Oceanogr.*, **16,** 1444–1446.

Large, W., and S. Pond, 1981: Open ocean momentum flux measurements in moderate to strong winds. *J. Phys. Oceanogr.*, **11,** 324–336.

Lazier, J. R. N., 1973: The renewal of Labrador Sea water. *Deep-Sea Res.*, **20,** 341–353.

Millot, C., and M. Crépon, 1981: Inertial oscillations on the continental shelf of the Gulf of Lions: Observation and theory. *J. Phys. Oceanogr.*, **11,** 639–657.

Petrie, B., and A. Isenor, 1985: The near-surface circulation and exchange in the Newfoundland Grand Banks region. *Atmos. Ocean,* **23,** 209–227.

Pollard, R. T., 1980: Properties of near-inertial oscillations. *J. Phys. Oceanogr.*, **10,** 385–398.

——, and R. C. Millard, 1970: Comparison between observed and simulated wind-generated inertial oscillations. *Deep-Sea Res.*, **17,** 813–821.

Price, J. F., 1983: Internal wave wake of a moving storm. Part I: Scales, energy budget and observations. *J. Phys. Oceanogr.*, **13,** 949–965.

Shay, L. K., and R. L. Elsberry, 1987: Near-inertial ocean response to hurricane Frederic. *J. Phys. Oceanogr.*, **17,** 1249–1269.

Smith, S. D., 1981: Factors for adjustment of wind speed over water to a 10 m height. Bedford Institute of Oceanography, Rep. Ser. BI-R-81-3, 29 pp.

Tang, C. L., 1979: Inertial waves in the Gulf of St. Lawrence: A study of geostrophic adjustment. *Atmos. Ocean,* **17,** 135–156.

Thompson, K. R., J. R. N. Lazier and B. Taylor, 1986: Wind-forced changes in Labrador Current transport. *J. Geophys. Res.*, **91,** 14 261–14 268.

Veronis, G., 1956: Partition of energy between geostrophic and non-geostrophic ocean motions. *Deep-Sea Res.*, **3,** 157–177.